An Integrated Electrocatalytic nESI-MS Platform for Quantification of Fatty Acid Isomers Directly from Untreated Biofluids

Kavyasree Chintalapudi[a] and Abraham K. Badu-Tawiah*[a]

Department of Chemistry and Biochemistry, The Ohio State University, Columbus OH 43210.
*Email: badu-tawiah.1@osu.edu

Abstract. Positional isomers of alkenes are frequently transparent to the mass spectrometer and difficult to provide convincing data to support their presence. This work focuses on the development of a new reactive nano-electrospray ionization (nESI) platform that utilizes non-inert metal electrodes (e.g., Ir and Ru) for rapid detection of fatty acids by mass spectrometry (MS), with concomitant localization of the C=C bond to differentiate fatty acid isomers. During the electrospray process, the electrical energy (direct current voltage) is harnessed for in-situ oxide formation on electrode surface via electro-oxidation. The as-formed surface oxides are found to facilitate in-situ epoxide formation at the C=C bond position and the products analyzed by MS in real-time. This phenomenon has been applied to analyze isomers of unsaturated fatty acids from complex serum samples, without pre-treatment.

Table of Contents

Experimental Methods

Chemicals and reagents. All chemicals and solvents were used without further purification, unless otherwise stated. Isosafrole (mixture of cis and trans), butylamine (nBu-NH_2) 99.5%, oleic acid (natural oleic acid, standard for GC), cis-Vaccenic acid (≥ 97%, capillary GC, oil), Linoleic acid (≥ 99%), and all the solvents (Methanol-MeOH, Acetonitrile (CH_3CN/ACN) - chromasolv® plus for HPLC) were purchased from Sigma-Aldrich. Ammonium Hydroxide (NH_4OH) was purchased from Fisher. Ethanol (EtOH) 200 proof was purchased from Decon Labs. Inc. Horse serum was purchased from Fischer Scientific. The deionized water with a resistivity of 18.2 MΩ-cm was obtained from a Milli-Q nano pure water filtration system purchased from Millipore Corporation.

Metal & Alloy Electrodes. Iridium Wire (0.006 in/ 0.15 mm diameter, 0.29990 ohms/cm) was purchased from Scientific Instrument Services, Inc. Pt/Ir (.006 in/ 34 Ga/ 0.15 mm diameter) and Pt/Ru LW6 (.006 Inch/ 34 Ga/ 0.15 mm diameter) were purchased from Hoover & Strong. Ag wire electrode holder for Glass OD size of 1.5mm was purchased from Warner Instruments. Pt wire (0.25 mm diameter, 99.99% trace metal basis) was purchased from the Chemistry Instrument Support Group (Internal Vendor at The Ohio State University).

X-Ray Photoelectron Spectroscopy (XPS). The Pt, Ir, Pt/Ir (90/10%) and Pt/Ru (95/5%) electrode surfaces were characterized by XPS measurements carried out with a Kratos Axis Ultra spectrometer, using focused monochromatized Al Kα radiation (hν = 1486.6 eV) as the X-ray source with 12 kV and 10 mA in a Spectrum-Analyzer Mode and Hybrid-Lens Mode. The analyzed area of the samples was set to 55 µm (Aperture Setting) of X-ray spot size. Peaks were recorded with a constant pass energy of 80 eV for survey and 20 eV for rest of the O1s, C1s, Ru3d, Ir4f and Pt4f. The pressure in the analysis chamber was $\sim 5 \times 10^{-8}$ Pa. For XPS measurement of each electrode sample, several XPS analyses were performed at different positions to make the results statistically reliable. The binding energy scale was calibrated for hydrocarbon contamination using the C1s peak at 285.0 eV. The electrode (used metal/alloy) samples were prepared after spraying samples from the n-ESI method using voltage of 1.5 kV. An unused Pt wire was used as control.

Operation of the nano-electrospray ionization (nESI). The emitter was mounted on to a stand with a copper clip to hold it in place. Electrical contact is made with nano-ESI solution via a metal/alloy electrode. High voltage for spraying was provided from the Mass Spectrometer. The sample was injected directly into the open end of the glass capillaries using long, thin gel-loader tips (Eppendorf, Hamburg). After loading the capillary with 10-20 μL of sample solution, the capillary was placed at 5-8 mm from the Mass Spectrometer's sampling orifice. A potential of 1.5 kV was applied at the capillary to start the spray. The flowrates of about 100 nL/min in this nESI allow the reactions to take place on this setup before the detection process.

In-capillary microextraction of fatty acids from serum. For direct biofluid analysis on this platform, liquid-liquid extraction of fatty acids using ethyl acetate was employed. This organic solvent was chosen because it is immiscible with water in the biofluids, allowing extraction of organic analytes (fatty acids, here) from the biofluid and suitable for nESI. Here, 5 µL of ethyl acetate was first placed in the sharp tip of the disposable glass capillary (I.D. 1.17 mm, O.D. 1.5 mm). A small volume (10 µL) of the biofluid sample spiked with selected analyte (**Table 1**) was then introduced on top of the ethyl acetate solvent (**Figure 4b**). A shake of the capillary (e.g., 3−5 strokes) initiates liquid−liquid extraction as well as aids in the removal of any air bubbles at the capillary tip. Ion signal from extracted analytes was not significantly affected by different number (n>3) of strokes. This shaking process is significantly different from slug-flow because it resulted in the disintegration of the biofluid into smaller compartments, which facilitated efficient extraction via increased interfacial contact with the extracting organic solvent. The high buoyancy of the less viscous ethyl acetate solvent (density 0.9 g/mL) ensures that clean extract is drawn to the sharp tip of the glass capillary for easy analysis by nESI MS.

To estimate extraction efficiency, we compared the average extracted ion intensity of the analyte (A, *m/z* 281 – oleic acid) in 98% ethyl acetate (EtOAc):H_2O with analyte signal derived from the liquid/liquid extraction processing utilizing 3 strokes of shaking. Serum spiked with oleic acid and an internal standard (oleic-d17 – IS, *m/z* 298) was used. By comparing signal (A/IS) from direct analysis to that recorded after liquid/liquid extraction, we were able to gauge the extraction efficiency at two different concentrations 200 µM and 300 µM, which turns out to be between 33 – 34 %.

Measurement of flow rate. To measure the flowrate, we filled the pulled tip glass capillary with 10 µL methanol/water (1:1) solution and sprayed for 10 min. Then the calculated mass difference of the capillary before (0.13325 g) and after (0.13246 g) the spray was used to estimate the volume of solvent sprayed when the density of solvent (0.9156 g/mL) was taken into account for the calculation. This subsequently enabled the flowrate of our experiments to be estimated. The calculated flowrate of ~100 nL/min is in good agreement with previously reported value (*Chem. Sci.* **2018**, 9, 5724-5729). Here, we have used the borosilicate glass capillaries (0.86 mm ID and 1.5 mm OD) and the pulled tip was measured to be <5 µm. All experiments were performed using a spray voltage of 1.5 kV.

Mass Spectrometry. Velos Pro linear ion trap mass spectrometer (Thermo Scientific, San Jose, CA, USA) was used for online reaction studies, operated in the full mass spectrum mode (mass range: 50-1000 Da). The tip of the capillary containing the metal/alloy electrode was held and positioned parallel to the MS inlet via a copper alligator clip, which was connected to power supply. MS parameters used were as follows: 200 °C capillary temperature, 3 microscans, and 60% S-lens voltage. Spray voltage was 1500 V unless otherwise specified. Helium gas was employed as the collision gas. The experiments were conducted in positive ion mode (isosafrole) and negative ion mode (fatty acids) respectively. Thermo Fisher Scientific Xcalibur version 2.2 software was applied for MS data collecting and processing. Tandem MS with collision-induced dissociation (CID) was utilized for analyte identification. Collision energy was tuned individually for each analyte to obtain the best possible MS/MS spectra. An isolation window of 1.0 times the (*m/z* units) and a normalized collision energy of 35%–40% (manufacturer's unit) were selected for the CID experiment.

Metal-oxide electrocatalysis: There has been a substantial literature on the formation of oxides on inert metals such as Ir and Ru metals upon application on voltage in contrast to those of Ag which only gives off electrons[1–5]. XANES spectra confirmed the formation of corresponding oxide species of Ir and Ru at 1.45 V , compared to the native metallic states at 0.05 V.[1] So, it should be possible to generate the corresponding metal oxide *in-situ* upon application of voltage during nano-ESI without the extensive bulk-phase synthesis of metal oxide catalysts. So, this will enable instantaneous and selective cleavage of C=C bonds on our electrospray based screening platform to facilitate the production of carbonyl compounds from alkenes in a matter of just few minutes with the use of non-inert electrodes such as Pure Ir, Pt/Ir (90/10%), Pt/Ru (95/5%). Metal oxide electrodes have the potential to act as anode for electrochemical oxidation as the electrode mechanism and the products obtained in the reaction depend on the anode material.[6] Electrical energy can be harnessed for *in-situ* modification of the electrode surface to generate electrochemical oxides, specific identity of which can be effectively controlled by varying the target electrode, pH background electrolytes, and other experimental parameters. So, these conditions will open new reaction pathways characteristic to the oxide catalysis reactions, which are not possible on inert electrodes.

Results and Discussion

Detection of oxidation product of isosafrole on the proposed platform

Figure S1. nano-ESI mass spectra of schiff base of piperonal when 200 µM of isosafrole was sprayed in the positive ion mode using Pt/Ir anode at DC voltage of 1.5 kV, showing the CID MS/MS spectra for *m/z* 206.

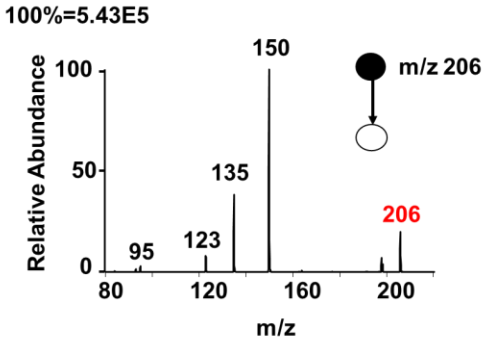

Scheme S1. Proposed mechanism of CID fragmentation pattern of protonated Schiff base of piperonal in positive ion mode MS/MS showing the pathway to major fragment ions *m/z* 150, 135, 123 and 95. Product ions at *m/z* 150 and 123 were formed from loss of butene (C_4H_8 – 56 Da) and subsequent loss of HCN (27 Da) from the parent ion. Product ion at *m/z* 150 was generated from the loss of n-butanimine (71 Da).

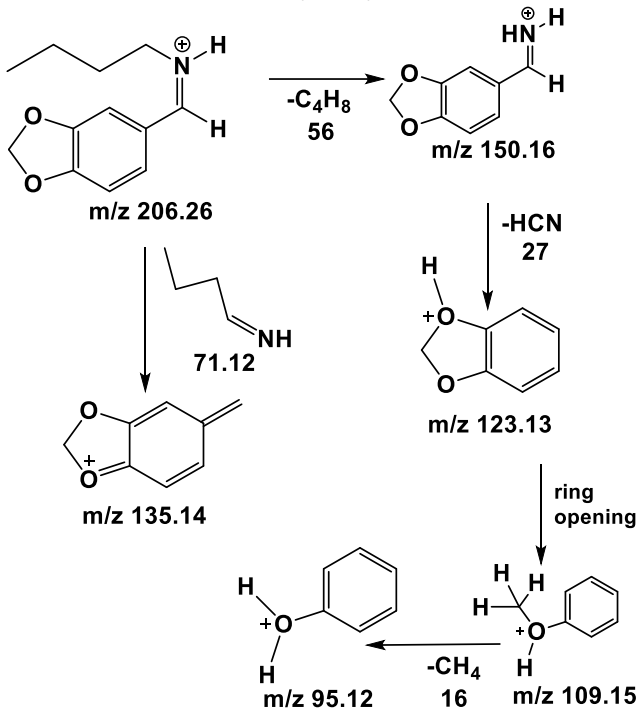

Figure S2. (i) nESI-MS analysis of isosafrole using Pt/Ir alloy anode and (ii) nESI-MS analysis of isosafrole depicting the emergence of expected product formation at *m/z* 204 after Pt anode is repeatedly used. This shows gradual change of surface properties from inert (first use) to reactive after many cycles of exposure to DC voltage and solvent.

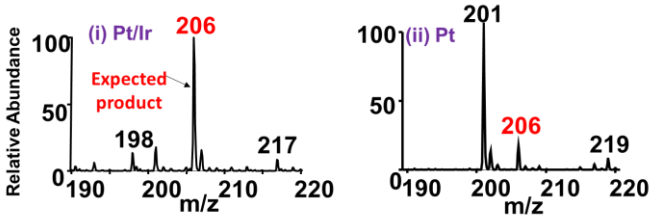

Mechanistic understanding on the electrochemical oxidation on metal oxides

There is an increasing attention towards the technique of using anodic and cathodic electrochemical reactions in the synthesis of organic compounds.[7] The electrode material is a very important parameter in the electrochemical oxidation of organics since the mechanism and products of some anodic reactions has been seen to be dependent on the anode material. The oxidation of organics can be classified into two main categories namely direct and indirect oxidation.[6] The electrocatalytic electrodes such as Platinum (Pt) can help in the direct oxidation whereas the indirect electrochemical oxidation can take place via surface mediators which remain fixed on the anode surface, where they are continuously regenerated.[7,8] There have been various mathematical models for anodic oxidation of organics on oxide electrodes with simultaneous oxygen evolution, one of which is shown below in **Scheme S2**.

Scheme S2. Schematic representation of the electrochemical oxidation of organics on oxide anodes (MO_x) forming the higher oxide (MO_{x+1}). 1. H_2O discharge; 2. Higher oxide formation; 3. Organics oxidation; 4. O_2 evolution.

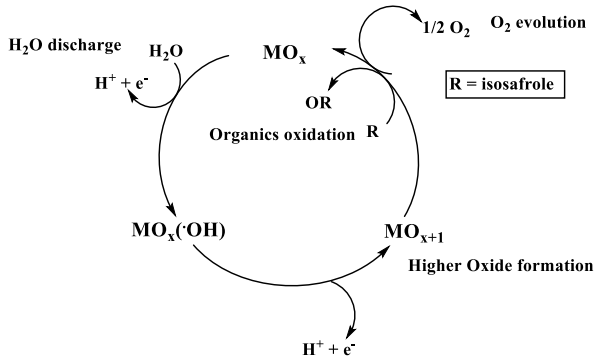

We propose that the electro-oxidation of C=C containing compounds proceeds via the epoxide intermediate, resulting in an oxidative cleavage type of reaction, without the need of any reductive/oxidative workup step as seen in case of ozonolysis. It has already been reported that bromide ion can be used in the halide ion mediated electrochemical oxidation for the epoxidation of olefins, where the epoxide and glycol products were isolated after chromatography.[9] From the data presented above we can clearly see an epoxide formation in case of C=C oxidation in oleic acid, but we couldn't characterize the corresponding epoxide intermediate in case of isosafrole. This can be attributed to the kinetics of the epoxidation and subsequent cleavage to give corresponding aldehyde functional group which might be very slow in case of oleic acid in comparison to isosafrole. We can also relate to the lower ionization efficiency of epoxide product in case of isosafrole, causing it to have the lower abundance in MS spectrum. We are still working on the characterization of the higher oxidation products seen in the spectrum. So, we propose that this oxidation is a combined effect of the O_2 from air and the *in-situ* generated metal oxides, catalyzing the electro-oxidation of alkene functional group studied in this work.

Oxygen binding abilities of many transition metals is well-known.[10,11] For example, Ir wire is the most corrosion-resistant wire known;[12] in this case the oxide film that forms on Ir surface is identified as playing an important role in the barrier against corrosion. Therefore, we consider the *native* surface structure of Ir and Ru as having an oxide film (MO_x). A discharge at the anode is expected to produce adsorbed hydroxyl radicals according to the equation;[13]

$$MO_x + H_2O \rightarrow MO_x(^{\bullet}OH) + H^+ + e^-$$

This physiosorbed active oxygen is a stronger oxidant capable of complete combustion of organics into CO_2.[14–16] A second active oxygen site is thought to be generated from the interaction of the physiosorbed hydroxyl radical with the oxygen already present in the oxide anode with possible transition from adsorbed $^{\bullet}OH$ to the lattice of the anode yielding a higher oxide, MO_{x+1}, with chemisorbed active oxygen.[13]

The experiments suggest Ir electrode is active toward isosafrole oxidation only in the presence of applied DC potential. This observation supports the existence of a transient active species similar to those generated in the physisorbed active oxygen surface, $MO_x(^{\bullet}OH)$. Indeed, in relatively low pH medium, such as that existing in the nESI process, the physisorbed hydroxyl radicals are found to dissociate to yield charged surface sites that eventually facilitate the formation of hydrated species generally represented as $MO_x(OH)_y$.[6,17] Although subject to further investigation, XPS analysis of used Ir electrode also did not reveal the presence of oxides. However, the unstable nature of $MO_x(OH)_y$ and $MO_x(^{\bullet}OH)$ may explain why limited or no oxide formation is found on Ir.

Optimization studies on the isosafrole oxidation system

Solvent Optimization. The isosafrole oxidation product intensity was compared in two solvents, acetonitrile (ACN) and MeOH/H_2O (1:1, v/v) at 100, 200 and 300 µM concentrations using Pt/Ir electrode charged at DC voltage of 1.5 kV.

MeOH/H_2O (1:1, v/v) was found to be the best solvent system due to comparatively higher intensity of the product. This can be rationalized by the fact that ACN is neither a protic solvent nor an O donor compared to MeOH.

Effect of Applied Voltage. The effect of spray voltage on the formation of protonated product ions was also investigated. **Figure S4** shows the optimum voltage occurred at 3 kV for all the electrodes. The intensity reached maximum at 3 kV and then the signal started to drop beyond that voltage, showing there might be an onset discharge formation occurring beyond voltage of 3 kV. In case of Ag and Pt, the formation of protonated Schiff base of piperonal $[M+H]^+$ (*m/z* 206) was observed starting from 1 kV, whereas for Pt/Ir and Pt/Ru, a stable signal started to be seen only from 1.5 kV. For monitoring the reaction for about 5-10 minutes, 1.5 kV was consistently chosen for all the preliminary studies since all the electrodes have shown a stable signal at this voltage and the solvent doesn't get consumed faster as seen in case of 3 kV.

Figure S3. A plot showing the effect of electrode and spray voltage on the intensity of protonated Schiff base of piperonal $[M+H]^+$ (*m/z* 206) when using MeOH/H_2O (1:1, v/v) as spray solvent.

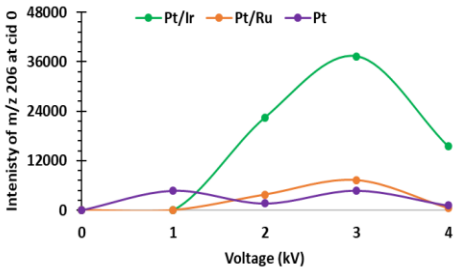

Effect of Concentration. Various concentrations ranging from 10, 30, 50, 100, 200, 300, 400 and 500 µM of (isosafrole/n-butylamine solution) were analysed by taking the Total Ion Chromatogram (TIC) at a specific time interval (1-2 min, 3-4min, with a CID of 33 units) for a comparative study upon various electrode surfaces at 1.5 kV. This was done to find if it is a surface heterogeneous reaction (i.e., any oxides formed on the surface of electrodes upon application of voltage) or if the effect is a homogeneous reaction occurring in bulk solution.
The hypothesis is that if isosafrole oxidation is heterogeneous, and product is arising only from electrode surface, then reaction rate should show a strong concentration effect. This means that the activity reaches saturation after a limit, due to all the sites getting occupied. Pure Ir shows a saturating point at 300 µM but not in case of Pure Pt and Pt/Ir in which case the signal continuously increased (**Figure S4**). So, we can conclude that depending on the electrode type, the oxidation of isosafrole can occur in solution or via *in-situ* formation of oxides on the surface of electrodes.

Figure S4. A plot showing the concentration dependent study of (isosafrole+nBu-NH2) to produce protonated Schiff base of piperonal $[M+H]^+$ (*m/z* 206) on Pt, Ir and Pt/Ir electrodes.

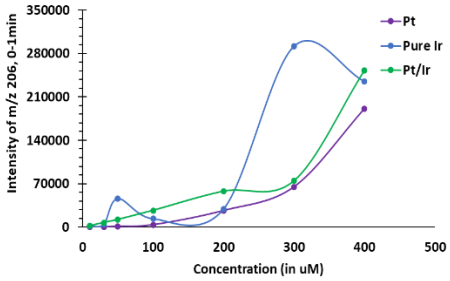

Figure S5. A plot showing the effect of Metal/alloy electrode on the intensity of protonated Schiff base of piperonal $[M+H]^+$ (*m/z* 206) produced when using MeOH/H_2O (1:1, v/v) as spray solvent, supported by the observed trend of oxophilicity among the metals of interest Pt < Ir < Ru.[1]

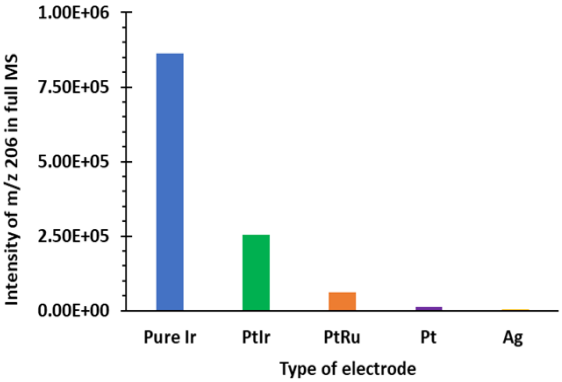

Effect of Spray Time. We performed a time resolved analysis to see at what time during the spray process, the reaction is most effective by continuous spraying and recording the full MS for about 5min. As shown in **Figure S6 a)**, the product ion intensity in case of pure Ir was about 100X higher than all the other electrodes, which has been expanded without in **Figure S6 b)** for Pt, Pt/Ir and Pt/Ru electrodes. This data shows that there is an instantaneous formation of product detected at 0.1 min of spraying. After 30 sec., however, there was about 10X increase in product ion signal, which remained relatively stable for the entire 4 min spray time. This shows that the electro-oxidative reaction happens in the capillary and not during the spray process.

Figure S6. a) Extracted ion chromatogram (XIC) showing the reaction progress for 4min to produce protonated Schiff base of piperonal [M+H]+ (*m/z* 206) on a) Pt, Ir, Pt/Ir and Pt/Ru b) Pt, Pt/Ir and Pt/Ru electrode (zoomed in XIC).

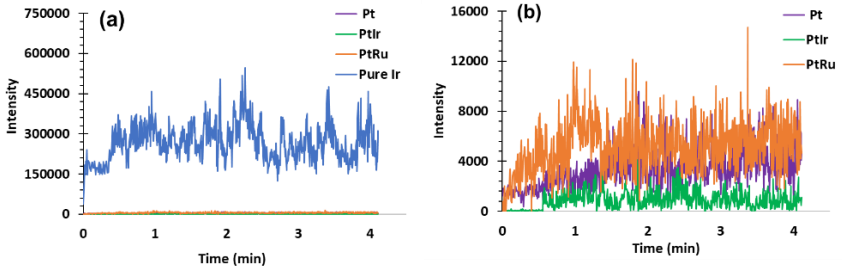

XPS studies

X-ray Photoelectron Spectroscopy (XPS): The Pt, Ir, Pt/Ir (90/10%) and Pt/Ru (95/5%) surfaces were characterized by XPS measurements carried out with a Kratos Axis Ultra spectrometer, using focused monochromatized Al Kα radiation (*hv* = 1486.6 eV) as the X-ray source with 12 kV and 10 mA in a Spectrum - Analyzer Mode and Hybrid - Lens Mode. The analyzed area of the samples was set to 55 μm (Aperture Setting) of X-ray spot size. Peaks were recorded with a constant pass energy of 80 eV for survey and 20 eV for rest of the O_{1s}, C_{1s}, Ru_{3d}, Ir_{4f} and Pt_{4f}. The pressure in the analysis chamber was $\sim 5 \times 10^{-8}$ Pa. For XPS measurement of each electrode sample, several XPS analyses were performed at different positions to make the results statistically reliable. The binding energy scale was calibrated from hydrocarbon contamination using the C1s peak at 285.0 eV. The electrode (used metal/alloy) samples were prepared from spraying samples from the n-ESI method using voltage of 1.5 kV. An unused Pt wire was used as control.

XPS studies were performed to investigate the nature of oxide formation on the electrodes over the time of the application of voltage during the experiments and to understand the effect of voltage on old (used) vs new (unused) electrodes. To identify if there is any permanent change or if the oxide is generated *in-situ* during the application of high voltage. We have obtained data using the Pt 4f, Ir 4f, Ru 3d, O1s peaks along with components on the Pt/Ir, Pt/Ru, Pt, Ir electrodes for both used and unused-with and without application of Voltage as shown in **Table S1**. Assigning of the peaks was made using the Gaussian and Lorentzian functions and their combination to find various oxidation states of Pt, Ir and Ru. We were able to characterize the elemental peaks, but there is a need to fine tune to find the minute peaks from expected metal oxides. After which can find the elemental ratios with respect to the controls to help us interpret the results clearly. The obtained Binding Energies (BE) of all the fitted peaks is shown in the **Table S1**.

Figure S7. Binding energy peaks for Pt 4f, Ir 4f and O1s on Pt/Ir electrode recorded to compare the used and unused electrodes with components.

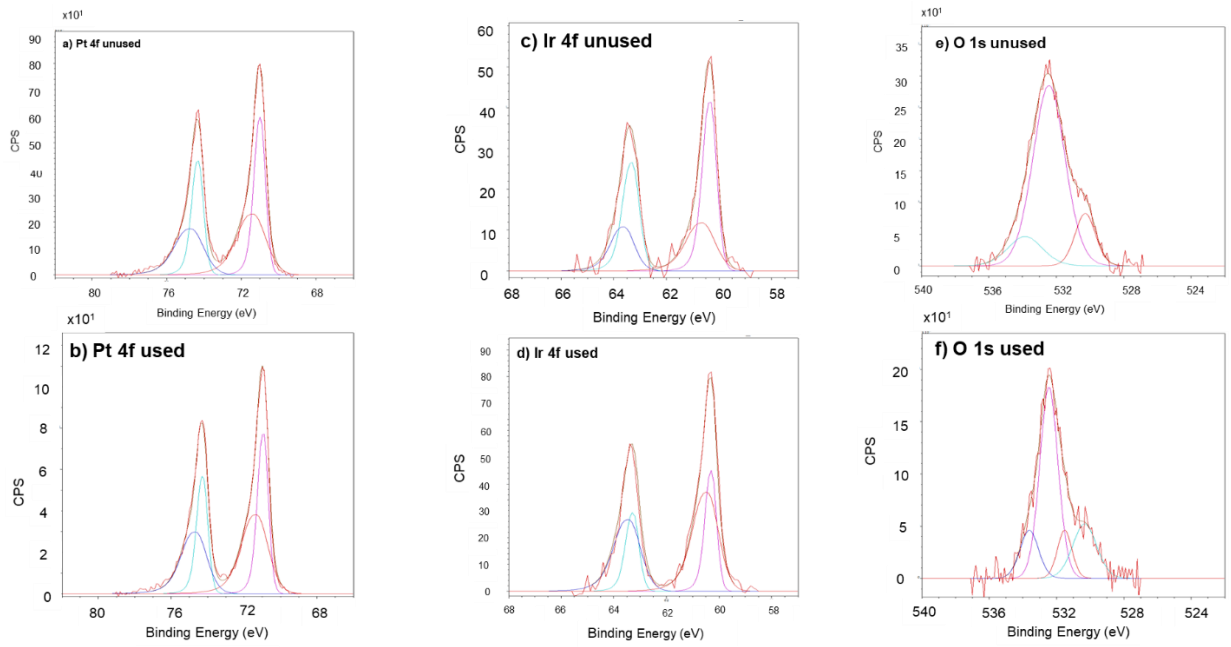

Figure S8. Experimental Binding Energy values for the new (unused) and used Pt/Ir electrode compared with some reported values[18] confirming the *in-situ* electrochemical oxidation process in our developed setup.

Standard Values (eV)				Experimental Values (eV)					
				New Electrode			Used Electrode		
	Ir $4f_{7/2}$	Ir $4f_{5/2}$	O 1s	Ir $4f_{7/2}$	Ir $4f_{5/2}$	O 1s	Ir $4f_{7/2}$	Ir $4f_{5/2}$	O 1s
Pure Ir	60.9	63.8	0	60.33	63.31	530.27	60.29	63.27	531.52
IrO_2	61.9	64.8	530.1	60.63	63.61	532.43	60.45	63.43	532.45

- Ir 4f metal BE shifts to lower values (~ 0.2 eV): increased screening of the nucleus
- O1s oxide BE shift from 530 to 531 : electron density is lost to oxygen
- *in-situ* electrochemical oxidation

Reference Values (eV)			
	Ir $4f_{7/2}$	Ir $4f_{5/2}$	O 1s
Ir (thermal oxidation)	61.9	64.8	530.0
Ir (electrochemical oxidation)	61.2	64.1	531.1

Oxides Type	O 1s Binding Energy (eV)
Transition metal oxides	530 +/- 0.5
Hydroxides	531.5
Absorbed water	533 +/- 1

Table S1. Results from photoemission spectra of the Pt 4f, Ru 3d, Ir 4f and O 1s level recorded from Pt/Ir, Pt/Ru, Ir and Pt electrodes

Electrode Type	Pt $4f_{7/2}$ BE (eV)	Pt $4f_{5/2}$ BE (eV)	Ru $3d_{5/2}$ BE (eV)	Ru $3d_{7/2}$ BE (eV)	Ir $4f_{7/2}$ BE (eV)	Ir $4f_{5/2}$ BE (eV)	O 1s BE (eV)
Pt/Ir unused	70.98 71.37	74.31 74.7	-	-	60.33 60.63	63.31 63.61	530.27 532.43 533.85
Pt/Ir used	70.93 71.33	74.26 74.66	-	-	60.29 60.45	63.27 63.43	530.33 531.52 532.45 533.62
Pt/Ru unused	71 71.42	74.33 74.75	279.98	284.15	-	-	530.62 532.68
Pt/Ru used	70.95 71.23	74.28 74.56	279.83	284	-	-	530.06 530.87 532.55 534.37
Ir unused	-	-	-	-	60.73 60.69	63.71 63.67	530.31 532.68 534.46
Ir used	-	-	-	-	60.75 60.76	63.73 63.74	531.57 532.75 534.16
Pt unused	70.94 71.39	74.27 74.72	-	-	-	-	530.47 532.98
Pt used	70.92 71.31	74.25 74.64	-	-	-	-	531.2 533.02 534.6

From the ranges of O1s binding energies observed, we know that there are 3 kinds of oxygen species: transition metal oxides: 530 +/- 0.5 eV, hydroxides: 531.5 eV and water of hydration/adsorbed water: 533 +/- 1 eV. The contribution from all these could result in the broad O1s signal and the O-to-Ir ratio to be larger than 2, the value expected for IrO_2. Also, the Ir 4f doublet of the main Ir(IV) species could overlap with a doublet from some Ir(VI), as in IrO_3, that is expected at slightly higher binding energies, resulting in 2 sets of Ir 4f doublets in our recorded spectra.[18] Although the results don't support the fact that there is an absolute permanent oxide layer formed on the surface of electrodes (not the exact values reported in literature as shown in Figure 11), we can note some expected trends in case of O1s peaks, the oxide BE shifts from 530 (unused) to 531(used) in Pt/Ir and Pt/Ru electrodes to higher values, supporting the fact that the electron density is lost to oxygen. Also, in case of the Ir 4f and Ru 3d peaks, Metal BE shifts to lesser values (-0.2 eV for Ir and -0.15 eV for Ru) due to increased screening of the nucleus. Another important point to note is that the electrochemically prepared metal oxides are less stable against dissolution compared to the thermally prepared ones, but the OER activity of the electrochemically prepared metal oxides is much higher than thermally prepared ones.[18] In case of Pure Pt electrode, there was hardly any shift in the BE values. Literature values (Figure 15) show the Pt 4f peaks at (71.1,74.5) for Pt-O, (71.2,74.5) for PtO_2 on Pt and O1s at (531.6, 530.0) for Pt-O and at 530.2 for PtO_2.[19] These results have been compared to that of photoemission spectral data of the Ir4f and O1s level recorded from commercial IrO_2 powder pressed into gold matrix[18] too.

The very narrow surface of the electrode wires exposed was also possessing a challenge for the good signals. Opening the aperture wide open has helped a bit in getting good signal. Due to the lesser concentration of Ru and Ir in Pt/Ru (95/5%) and Pt/Ir (90/10%) wires, characterizing the amount of oxide formations from the peaks was getting very difficult. So, performed this again with pure Ir and Pure Pt electrodes. The surface contamination of C and oxygen was much greater than the actual O signal from the oxides. Through XPS analysis, we have confirmed the *in-situ formation*

of the corresponding *nascent oxides* while using Ir and Ru electrodes in nESI-MS, upon the application of high voltage since permanent change onto the surface of the electrodes was not clear from the above data.

Application of the optimized setup on the study of fatty acids

Scheme S3. Proposed mechanism of expected oxidative cleavage of oleic acid on our platform, resulting in its epoxidation in negative ion mode instead opening new pathway for structural identification of isomeric fatty acids.

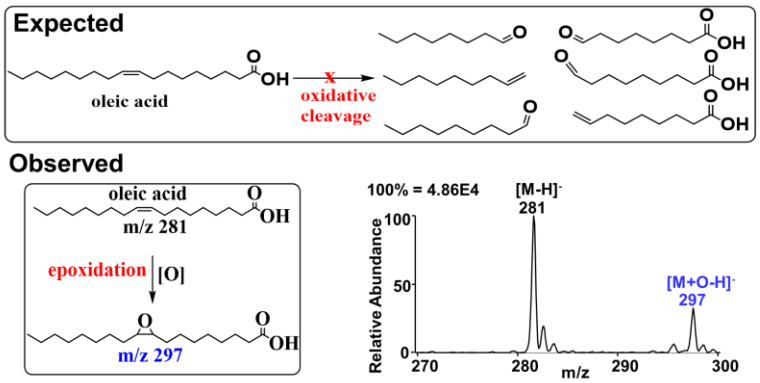

Figure S9. nano-ESI mass spectra of 200 µM oleic acid in the negative ion mode at DC voltage of 1.5 kV, showing the oleic acid at *m/z* 281 and oleic acid epoxide at *m/z* 297.

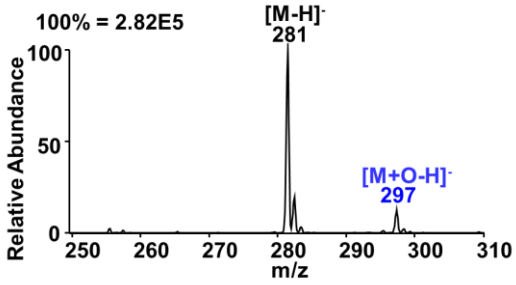

Figure S10. Comparison of how other MS additives like b) ammonium acetate ($NH_4CO_2CH_3$) and c) ammonium carbonate ($(NH_4)_2CO_3$) effect the efficiency of the epoxidation reaction with that of a) 1% NH_4OH.

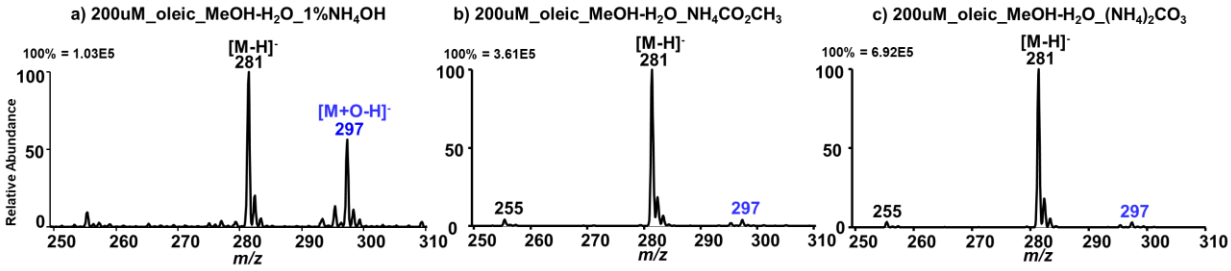

Figure S11. Nano-ESI mass spectra of 200 µM oleic acid using traditional nESI-MS conditions involving a) Ag and b) Pt electrodes and c) Pt (in presence of 1% NH_4OH) in the negative ion mode at DC voltage of 1.5 kV.

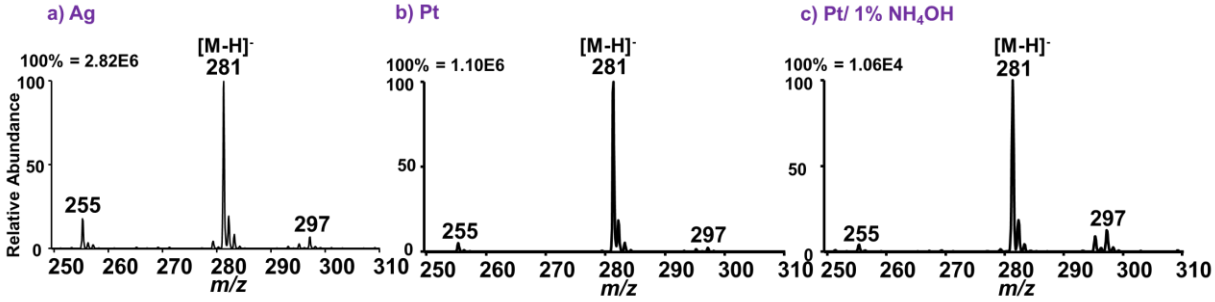

Figure S12. Tandem MS analysis of oleic acid epoxide at *m/z* 297 producing the fragment ions at *m/z* 155, 171, 183, 253 and 279 in presence of 1% NH_4OH. Upon CID, we could also note that the intensity in the fragment at *m/z* 183 has drastically decreased when the reaction was carried out in presence of the 1% NH_4OH.

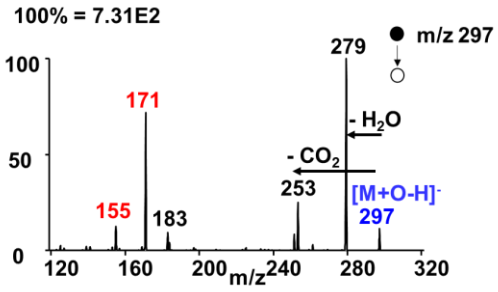

Scheme S4. Proposed mechanism of CID fragmentation pattern of deprotonated oleic acid after epoxidation in negative ion mode MS/MS showing the pathway to major fragment ions termed as diagnostic ions at *m/z* 171 and 155.

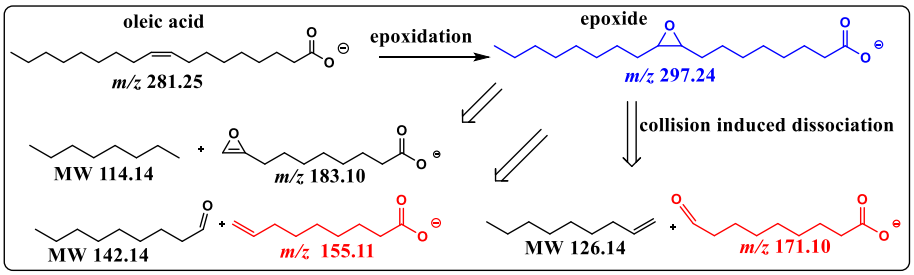

For one fragmentation channel, an ethylene group was formed at the site of cleavage via intramolecular hydrogen transfer and in the other complementary fragment, an aldehyde group was generated at the distal end. In each pair of products, only the ions at 155, 171 and 183 each carrying a negative charge at the carboxyl group (COO^-) can be detected by MS. We can see that only two ions out of the four fragments can be detected, which are termed diagnostic ions as they can be used to accurately pinpoint the C=C location. The other product ions at *m/z* 279 and 253 were formed following the loss of H_2O (18 Da) and CO_2 (44 Da) from parent epoxide ion (*m/z* 297). The *m/z* 183 was formed from the cleavage of the neutral hydrocarbon chain attached to the epoxide ring.

Figure S13. Test for the presence of H_2O_2 in the cathodic experiment that could be generated *in-situ* after the application of the negative potential (10% KI reaction with H_2O_2). i) No color change upon addition of 3 drops of 10% KI to MeOH/H_2O solution. ii) The solution in the capillary slowly turns yellow after about 10-15 min (beyond the range of our spray time) in which acetic acid has been added to the above solution, showing that there has been an insignificant amount of peroxides generated during the spray process in the negative mode during our spray conditions.

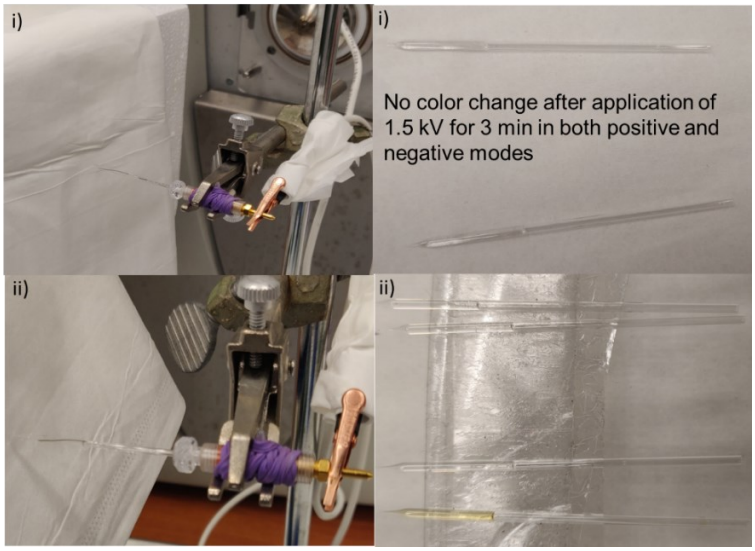

Figure S14. Full MS of cis-vaccenic acid in presence of 1% NH_4OH base in MeOH-H_2O (1:1) on Ir electrode

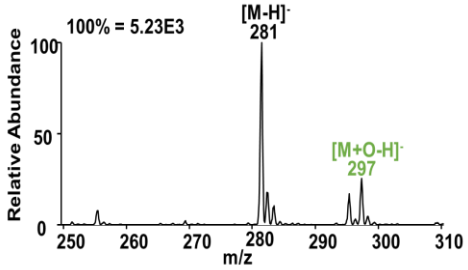

Scheme S5. Proposed mechanism of CID fragmentation pattern of deprotonated cis-vaccenic acid after epoxidation in negative ion mode MS/MS showing the pathway to major diagnostic fragment ions at *m/z* 183 and 199 respectively.

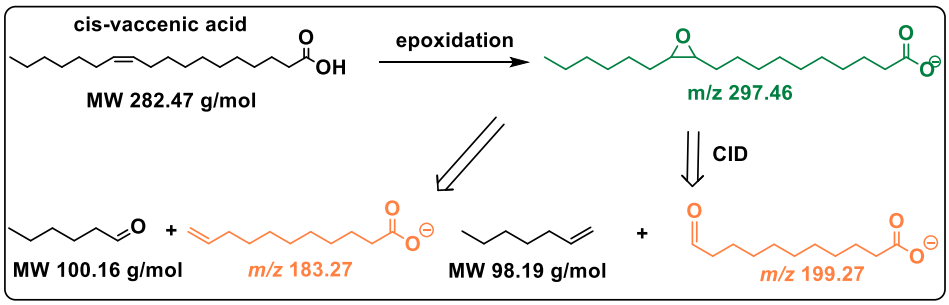

Figure S15. Full MS of a 1:1 mixture of oleic: vaccenic acids on Ir electrode in MeOH-H_2O (1:1)

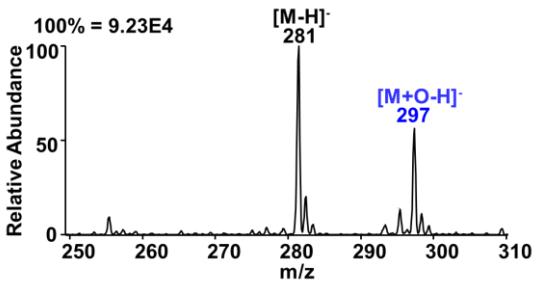

Scheme S6. Proposed mechanism of CID fragmentation pattern of deprotonated linoleic acid after di-epoxide *m/z* 311 in negative ion mode MS/MS showing the pathway to various fragment ions, highlighting the compounds that can be detected in the negative mode.

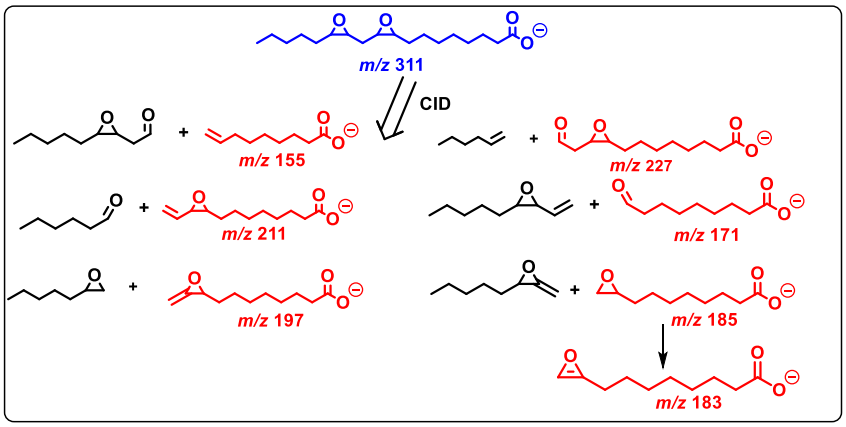

Figure S16. Tandem MS analysis of di-epoxide of linoleic acid epoxide at *m/z* 311 producing various fragment ions at *m/z* 155, 171, 183, 197,195, 211, 267 and 293.

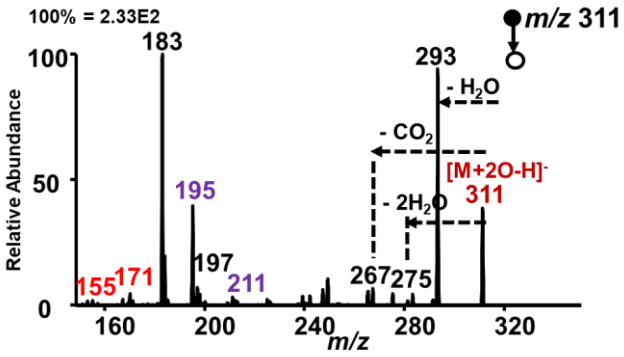

Table S2. Fragment ions specific to the C=C position(s) for Unsaturated Fatty acids studied.

Fatty acid	Double-bond position	Parent ion $[M+O-H]^-$	Fragment ions (*m/z*)
FA 18:1	9	297	171 & 155
FA 18:1	11	297	199 & 183
FA 18:2	9 and 12	295	171 & 155, 195 & 211

Figure S17. 200 µM of i) oleic acid in methanol/water (1:1, vol./vol.), ii) oleic acid in methanol/water (1:1, vol./vol.) in the presence of 1% NH_4OH, and iii) isosafrole + butylamine dissolved in MeOH/H_2O (1:1, , vol./vol.) during non-contact native nESI MS analysis to contact, oxidative spray conditions (using Ir electrode in all cases) confirming the claim that there is a formation of oxidation product in the oxidative conditions where as we can have the species in their native conditions using non-contact spray.

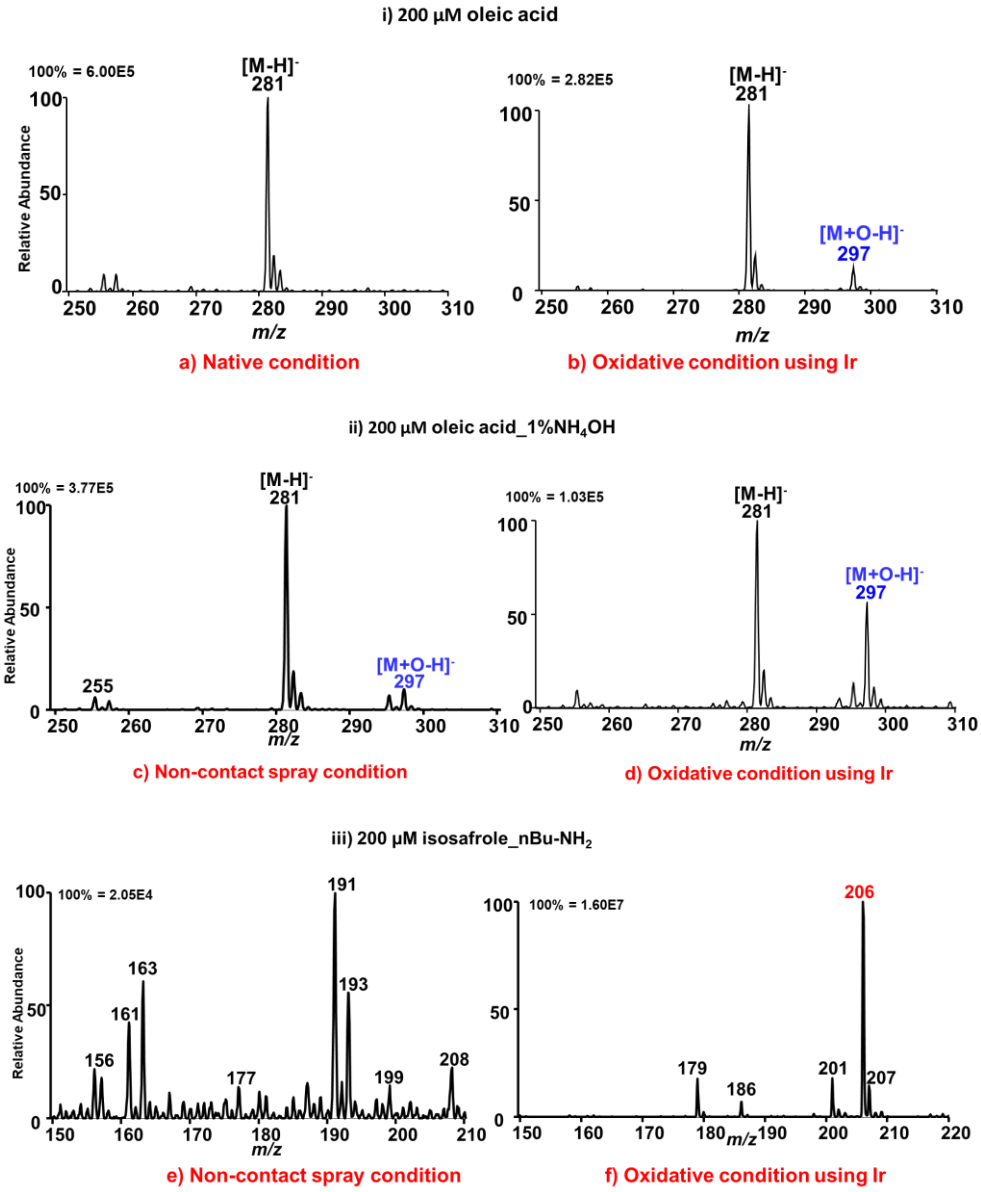

Rapid identification of Free Fatty Acids (FFAs) in Serum

Figure S18. Using oleic acid, we compared the average extracted ion chromatogram (XIC) signal of the analyte (A, *m/z* 281) in 98% ethyl acetate (EtOAc):H_2O with that of extracted from spiked serum in presence of internal standard (oleic-d17 – IS, *m/z* 298) sample as shown below to gauge the extraction efficiency, which turns out to be around 34-35 % as shown below at two concentrations, a) 200 µM and b) 300 µM.

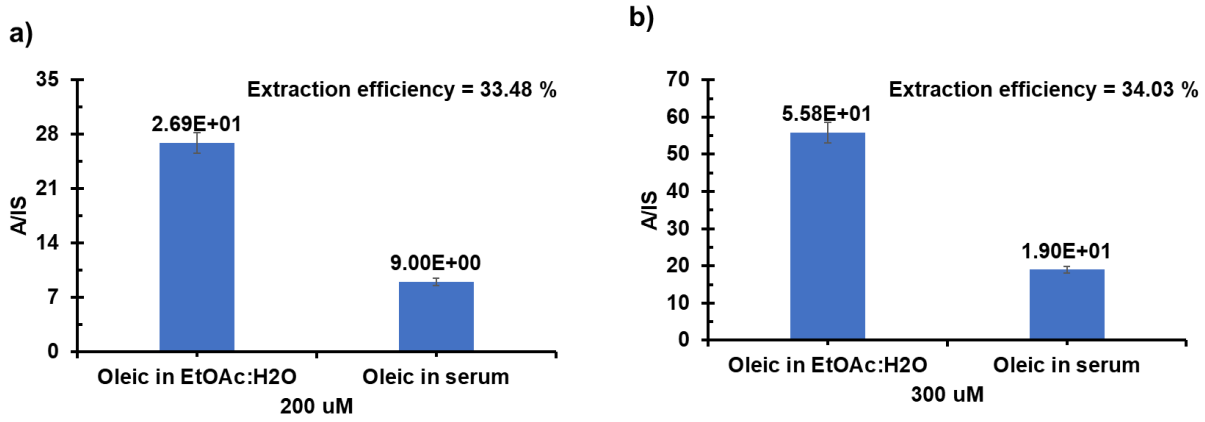

Figure S19. MS spectra confirming the detection of the most prevalent fatty acids in horse serum: FAs a) 18:3 (linolenic) b) 16:1(palmitoleic), c) 18:0 (stearic) and d)16:0 (palmitic) along with that of oleic (18:1) and linoleic acid (18:2) shown earlier.

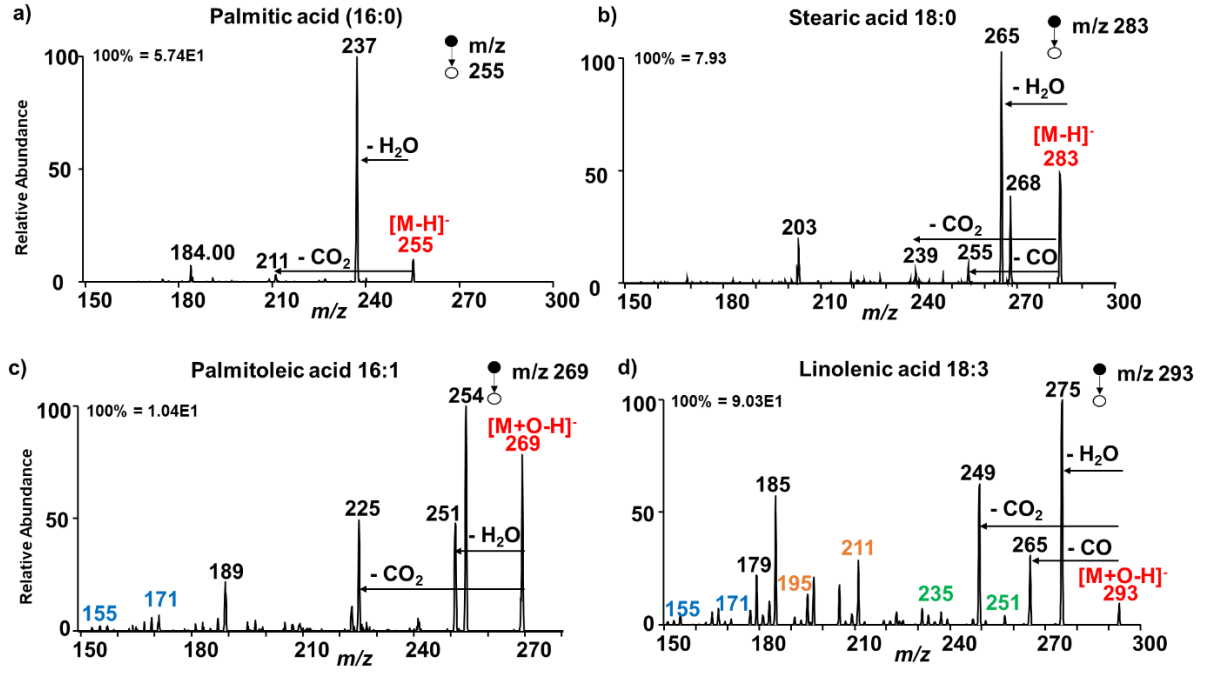

Figure S20. a) Intensities of the MS/MS product ions monitored for oleic acid (*m/z* 297) extracted from serum, where the inherent cis-vaccenic acid's diagnostic peaks have also been recorded on Ir electrode using in-capillary micro-extraction setup. b) Intensities of the MS/MS product ions monitored for linoleic acid (*m/z* 295) in serum on Ir electrode.

1.5 kV used for nESI. This spectrum was recorded in pure serum without doping using the in-capillary micro-extraction setup.

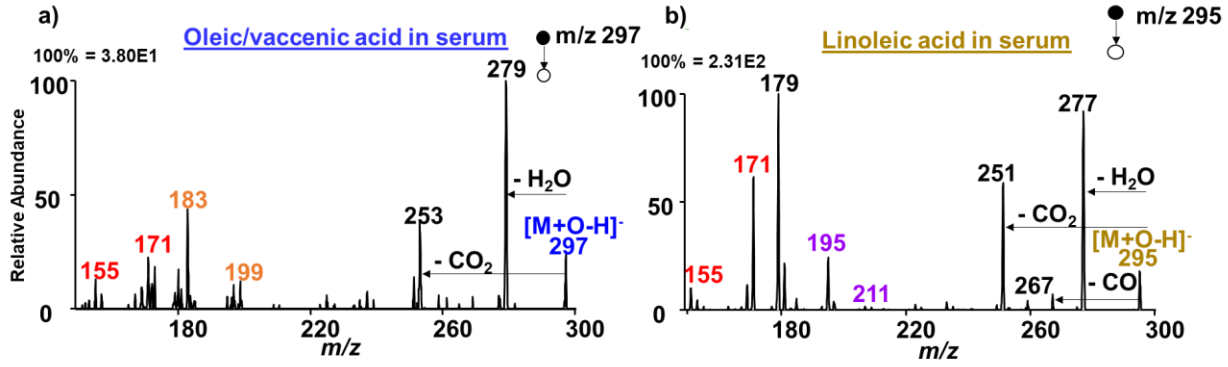

Figure S21. Calibration curves for the fatty acids spiked in serum in presence of an internal standard (C18:1-d17) with raw data points for their quantification in serum, a) oleic acid b) cis-vaccenic acid and c) linoleic acid respectively.

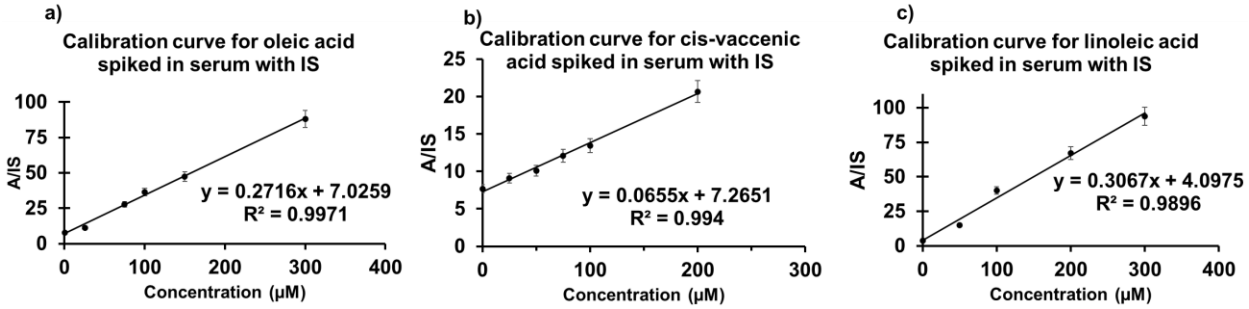

References

1 N. Danilovic, R. Subbaraman, K.-C. Chang, S. H. Chang, Y. J. Kang, J. Snyder, A. P. Paulikas, D. Strmcnik, Y.-T. Kim, D. Myers, V. R. Stamenkovic and N. M. Markovic, *J. Phys. Chem. Lett.*, 2014, **5**, 2474–2478.
2 A. Li, Q. Luo, S.-J. Park and R. G. Cooks, *Angew. Chem. Int. Ed.*, 2014, **53**, 3147–3150.
3 S. Cherevko, *Journal of Electroanalytical Chemistry*, 2017, **787**, 11–13.
4 R. Kötz, H. Neff and S. Stucki, *J. Electrochem. Soc.*, 1984, **131**, 72–77.
5 O. Simond and Ch. Comninellis, *Electrochimica Acta*, 1997, **42**, 2013–2018.
6 *Electrochimica Acta*, 1997, **42**, 2009–2012.
7 E. Lodowicks and F. Beck, *Chem. Eng. Technol.*, 1994, **17**, 338–347.
8 M. E. G. Lyons, C. H. Lyons, A. Michas and P. N. Bartlett, *Journal of Electroanalytical Chemistry*, 1993, **351**, 245–258.
9 S. Torii, K. Uneyama and K. Ueda, *J. Org. Chem.*, 1984, **49**, 1830–1832.
10 R. Subbaraman, D. Tripkovic, K.-C. Chang, D. Strmcnik, A. P. Paulikas, P. Hirunsit, M. Chan, J. Greeley, V. Stamenkovic and N. M. Markovic, *Nature Mater*, 2012, **11**, 550–557.
11 K. P. Kepp, *Inorg. Chem.*, 2016, **55**, 9461–9470.
12 J. Matthey, A History of Iridium, https://www.technology.matthey.com/article/31/1/32-41/, (accessed January 10, 2020).
13 *Electrochimica Acta*, 1994, **39**, 1857–1862.
14 B. Nasr and G. Abdelatif, *The Canadian Journal of Chemical Engineering*, 2009, **87**, 78–84.
15 W. H. Glaze, J.-W. Kang and D. H. Chapin, *Ozone: Science & Engineering*, 1987, **9**, 335–352.
16 R. Parsons and T. VanderNoot, *Journal of Electroanalytical Chemistry and Interfacial Electrochemistry*, 1988, **257**, 9–45.
17 G. W. Simmons and B. C. Beard, *J. Phys. Chem.*, 1987, **91**, 1143–1148.
18 M. Peuckert, *Surface Science*, 1984, **144**, 451–464.
19 C. R. Parkinson, M. Walker and C. F. McConville, *Surface Science*, 2003, **545**, 19–33.